Received: 24 June 2016 | Revised: 23 April 2017 | Accepted: 5 June 2017
DOI: 10.1002/term.2494

WILEY

RESEARCH ARTICLE

Multimodal-3D imaging based on μMRI and μCT techniques bridges the gap with histology in visualization of the bone regeneration process

R. Sinibaldi[1,2] | **A. Conti**[1] | **B. Sinjari**[3] | **S. Spadone**[1] | **R. Pecci**[4] | **M. Palombo**[5,6] | **V.S. Komlev**[7] | **M.G. Ortore**[8] | **G. Tromba**[9] | **S. Capuani**[10] | **R. Guidotti**[1] | **F. De Luca**[5] | **S. Caputi**[3] | **T. Traini**[3] | **S. Della Penna**[1,11]

[1] Department of Neuroscience, Imaging and Clinical Sciences, G. D′Annunzio University of Chieti-Pescara, Chieti, Italy

[2] Multimodal3D s.r.l., Rome, Italy

[3] Department of Medical and Oral Sciences and Biotechnologies, G. D′Annunzio University of Chieti and Pescara, Chieti, Italy

[4] Department of Technologies and Health, Istituto Superiore di Sanità, Rome, Italy

[5] Department of Physics, Sapienza University of Rome, Rome, Italy

[6] CEA/DSV/I2BM, MIRCen, Fontenay-aux-Roses, France

[7] A.A. Baikov Institute of Metallurgy and Materials Science, Russian Academy of Sciences, Moscow, Russian Federation

[8] Department of Life and Environmental Science, Marche Polytechnic University, Ancona, Italy

[9] Elettra Sincrotrone Trieste, Trieste, Italy

[10] CNR (Institute for Complex Systems) c/o Physics Department Sapienza University of Rome, Rome, Italy

[11] Institute for Advanced Biomedical Technologies, G. D′Annunzio University of Chieti-Pescara, Chieti, Italy

Correspondence
Stefania Della Penna, Department of Neuroscience, Imaging and Clinical Sciences, G. D′Annunzio University of Chieti-Pescara, Via dei Vestini 31, I-66100 Chieti, Italy; or Institute for Advanced Biomedical Technologies, G. D′Annunzio University of Chieti-Pescara, Via dei Vestini 31, I-66100 Chieti, Italy.
Email: stefania.dellapenna@itab.unich.it

Funding information
Networks for high education - P.O.F.S.E. Abruzzo 2007-2013

Abstract

Bone repair/regeneration is usually investigated through X-ray computed microtomography (μCT) supported by histology of extracted samples, to analyse biomaterial structure and new bone formation processes. Magnetic resonance imaging (μMRI) shows a richer tissue contrast than μCT, despite at lower resolution, and could be combined with μCT in the perspective of conducting non-destructive 3D investigations of bone. A pipeline designed to combine μMRI and μCT images of bone samples is here described and applied on samples of extracted human jawbone core following bone graft. We optimized the coregistration procedure between μCT and μMRI images to avoid bias due to the different resolutions and contrasts. Furthermore, we used an Adaptive Multivariate Clustering, grouping homologous voxels in the coregistered images, to visualize different tissue types within a fused 3D metastructure. The tissue grouping matched the 2D histology applied only on 1 slice, thus extending the histology labelling in 3D. Specifically, in all samples, we could separate and map 2 types of regenerated bone, calcified tissue, soft tissues, and/or fat and marrow space. Remarkably, μMRI and μCT alone were not able to separate the 2 types of regenerated bone. Finally, we computed volumes of each tissue in the 3D metastructures, which might be exploited by quantitative simulation. The 3D metastructure obtained through our pipeline represents a first step to bridge the gap between the quality of information obtained from 2D optical microscopy and the 3D mapping of the bone tissue heterogeneity and could allow researchers and clinicians to non-destructively characterize and follow-up bone regeneration.

KEYWORDS

3D mapping, bone regeneration, image coregistration, micro magnetic resonance imaging, multimodal imaging, multivariate clustering, X-ray computed microtomography

1 | INTRODUCTION

In the last years, the research towards novel biomaterials both for orthopaedic and dental applications has been receiving growing attention, driven by the requirement to improve both the healing behaviour of tissues around implants and the quality of life in patients. A natural application for these materials is maxillofacial surgery, as the number of implants is constantly increasing. Despite their medium dimensions and volumes, jaw and mandible are highly load-bearing structures (Hellmich, Kober, & Erdmann, 2008) and the probability of implant failure is considerable (Chee & Jivraj, 2007). In the case of critical bone defect, the use of bone substitute biomaterials (BSBs) for bone tissue replacement and/or repair represents the most used strategies in dentistry. The success or failure of a dental implant depends on the biological and clinical properties of BSBs (Komlev et al., 2010; Miri et al., 2016; Torres et al., 2007), which together with the host bone quality determine the regeneration process (Karsdal, Martin, Bollerslev, Christiansen, & Henriksen, 2007). At present, it is possible to determine the actual bone strength of an individual to assess the risks of bone fracture only locally through invasive methods (Farr et al., 2014). Using quantitative parameters to obtain a better understanding of biological reaction to artificial structure, under different tissue conditions, is fundamental for an accurate investigation of the factors influencing the fracture risk and for an effective follow-up (Sievanen, Kannus, & Jarvinen, 2007).

Currently, the standard technique for quantitative evaluation of biomaterial biodegradation and bone formation is 2D histomorphometry, which is based on serial sectioning and staining of the sample, analysed through optical microscopy (Giannoni et al., 2008). Histomorphometry provides images with an in-plane resolution better than 1 μm, a slice thickness ranging between 10 and 50 μm, with high contrast between different tissues, but it is invasive, significant sample parts can be destroyed during sectioning, and only the observation of 2D structures in small samples is allowed. This limitation paved the way to 3D microimaging as a promising methodology to investigate bone microanatomy also by noninvasive in vivo assessment (Khosla et al., 2006) supported by 2D histomorphometry, which is often used to validate 3D structures revealed by tomographic techniques (Giannoni et al., 2008), even in clinical practice.

High-resolution X-ray synchrotron radiation microCT (SRμCT) features a 3D voxel resolution similar to 2D microscopy (Withers, 2007). Nonetheless, due to the low X-ray absorption coefficient of biological samples, the SRμCT contrast between different tissues in regenerated oral bone (e.g., between the low mineralized bones and the marrow) is worse than microscopy. Thus, 3D histomorphometry is altered by the colonization of porous structure by marrow cells, bone regeneration, angiogenesis, and BSBs degradation.

Micromagnetic resonance imaging (μMRI) is the best diagnostic modality for the analysis of images of soft tissues in the body. Moreover, μMRI is also used to diagnose degenerative disc diseases and to reveal stress fracture in bone and cartilage. Specifically, μMRI allows investigation of the trabecular bone networks providing precious information on the physiological and structural changes of bone quality, such as the degree of vascularization (Vandoorne et al., 2010) and of bone calcification, also by means of quantitative parameters correlated to μCT parameters (Wurnig et al., 2014). Despite its worse spatial resolution, μMRI produces images with a higher contrast, showing richer bone tissue variability compared to SRμCT.

Here, a new multimodal approach aiming at bridging the gap between high-quality 2D optical imaging and 3D microtomographic techniques is presented. Our main goal is the quantitative 3D imaging of new bone tissue. The presented method is tested over ex vivo bone cores obtained after bone graft in human maxilla. We exploit the potential of combining images from μMRI and SRμCT to increase the imaging contrast of biological tissues and to obtain their 3D spatial distribution. Specifically, we combine the images through an optimized 3D registration and an automatic algorithm for multivariate clustering analysis of 3D images, and we label clusters through comparison with histological references.

2 | MATERIALS AND METHODS

2.1 | Biomaterial and surgical protocol

The investigated samples were retrieved from three patients (two females ~50 years old, sample C-1 and C-2, and one male 65 years old, sample C-3) who presented a partial edentulous maxilla and were candidate for implant placing after a bone graft. The patients signed their informed consent for the treatment plan and for the sample collection according to the ethical principles of the Declaration of Helsinki including the World Medical Association. A cone beam computed tomography was performed before surgery to plan the treatments. The bone cores used in this study were obtained using a trephine bur of 3 mm diameter during surgery performed to place titanium screw implants. The three samples were retrieved after 6 months healing process following augmentation of maxillary sinus floor with particles of anorganic bovine bone (Bio-Oss, Geistlich, Wolhusen, Switzerland) mixed with venous blood and fibrin sponge (Spongostan dental, Ferrosan Medical Devices A/S, S.borg, Denmark). The extracted jawbone cores (in the following referred as C-1, C-2, and C-3) were fixed in 10% buffered formalin at pH 7.1, washed in sodium phosphate buffer solution at pH 7.2 and dehydrated in graded alcohols. The cores were small cylinders with a length between 3.5 and 4.5 mm and a diameter ~ 2.5 mm.

2.2 | X-ray computed microtomography

The sample was analysed by SRμCT at the SYRMEP beam line of the Elettra Synchrotron Laboratory (Tromba, Abrami, et al., 2010) with a monochromatic beam of 23 keV in free propagation-based phase contrast imaging. The chosen detector was a water-cooled CCD camera by Photonic Science, model VHR, 4008 × 2672 full frame, used in 2 × 2 binning mode (resulting in a 9 μm isotropic voxel) and coupled to a Gadolinium Oxysulphide scintillator placed on a fibre optic taper. In addition to the specimens, a water sample was measured in the same conditions to calculate the Hounsfield units (HUs) of the samples. Two standard samples with density similar to trabecular bone (100 mg/cm^3 and 400 mg/cm^3) were measured to find calibration parameters and calculate sample mineral density from the HU (Genant et al., 1996). The equation $HU = 1.475\ \rho + 19.7$ was used to calculate the mineral density ρ of each sample. The bone cores were then scanned in a parafilm cap to prevent desiccation and fixed on the sample holder with plasticine. Scans were reconstructed by applying the conventional filtered back projection procedure (BPI) after preprocessing the original dataset with the application of the TIE-based (transport of intensity equation) phase-retrieval (PR) algorithm (Gureyev, Mohammadi, Nesterets, Dullin, & Tromba, 2013). Application of PR techniques on biological samples is used to improve the visualization of structures and of details within complex geometries, which could be hardly detected in standard BPI.

2.3 | Micromagnetic resonance imaging

μMRI measurements were carried out on a Bruker 9.4 T Avance spectrometer, operating with a microimaging probe (10 mm internal diameter) and equipped with a BGU2 gradient unit (max gradient strength of 1,200 mT/m). Spin echo images were acquired by a Multi Slice Multi Echo sequence (repetition time T_R = 2,500 ms, matrix 256 × 256, in-plane resolution 18 × 18 μm^2 and slice thickness 200 μm, 100 scans, 22 slices) at four different echo times T_E (4.8, 9.5, 14.3, and 19.1 ms). We acquired T_2^{APP}-weighted MR images, because the apparent transverse relaxation time T_2^{APP} is sensitive to the internal magnetic field gradient (IMFG) generated at the interface between tissue and bone, which is related to different calcification levels of bone matrix and dimension of pores filled with bone marrow, which is mainly composed of fat and water (Di Pietro, Palombo, & Capuani, 2014). As a consequence, the spin-echo decay S as a function of T_E is described as $S(T_E) = S(0)^*\exp(-T_E/T_2^{APP})$, where S(0) is the signal at $T_E = 0$ and T_2^{APP} depends on the spin–spin relaxation time T_2 and on the IMFG experienced by bone marrow protons diffusing at the interfaces between bone marrow and solid bone in each pore (De Santis, Rebuzzi, Di Pietro, Maraviglia, & Capuani, 2010; Rebuzzi et al., 2013). Therefore, spin-echo images obtained in bone are weighted by T_2^{APP} that depends on several parameters related to different cancellous bone features (for more details about T_2^{APP}, see Supporting Information).

The μMRI acquisition was performed on the sample immersed in water to increase the image contrast of the porous mineral network. Indeed, water molecules in different cancellous bone zones are characterized by different values of T_2^{APP}, depending on different local water concentrations and/or on different local micromorphology.

2.4 | Histological investigation

The light microscopy investigation was performed after the other imaging scans, as the preparation of the samples for this technique is invasive and destructive. The samples were embedded in resin (LR White, London Resin, Berkshire, UK) and transverse undecalcified cut sections of (50 ± 20) μm were prepared by using the TT System (TMA2, Grottammare, Italy) and ground down to about (35 ± 10) μm using the EXAKT grinding system (EXAKT Vertriebs Gmbh, Norderstedt, Germany). The sections were double stained with basic methylene and blue-azure II. We selected this stain, noted also as methylene blue-azure B, because it contains blue cations attracted by cartilage matrix, or mast cell granules and red anions attracted by proteins. DNA and rRNA are then stained blue, but structures with high density of anionic sites, such as mast cell granules and cartilage matrix, are coloured reddish-purple (Kierman, 2010). The chosen method was adopted to study different human tissues in epoxy resin (Fritsch, 1989). The samples were studied in normal transmitted light using a bright field light microscope (Axiolab, Carl Zeiss, Jena, Germany). The optical system was connected to a high-resolution CCD-IRIS digital camera (Sony DXC-107-A, Tokyo, Japan), and the images were captured using Image-Pro Plus 6.0 (Media Cybernetics Inc., Bethesda, MD, USA). The in-plane resolution was 1.6 μm.

2.5 | Normalized mutual information-based registration

Strategies for image registration aim at finding the set of parameters *t*, defining the transformation *T* that overlaps one image *A* onto a second image *B* maximizing their spatial correspondence, then B = TA. *T* is obtained from the product of two independent transformations: a zoom transformation, to match the different resolutions of the two techniques, and a rigid transformation defined by three translation and three rotation parameters related to the reference system of image *A*.

To obtain the best estimate of the transformation T, an iterative procedure maximizing a cost function is applied over several Regions of Interest (ROIs) of the reference image B (instead of the whole image to save computational time) and starting from different initial guesses. A suitable cost function is the normalized mutual information (*NMI*), which is less sensitive than mutual information (Studholme, Hill, & Hawkes, 1999) to the size of the overlapping parts of the two 3D structures.

2.6 | Minimization and grouping procedures

We used adaptive simulated annealing (ASA) to find the best set of parameters of the transformation *T** maximizing the NMI. NMI is a not convex function of the set of parameters *t*, and ASA is a robust method to avoid trapping in local minima and funnels (Press, Flannery, Teukolsky, & Vetterling, 1991), which could be present in the parameters space when coregistering 3D image stacks. At each iteration, the transformation *T** is estimated and applied to image A. Notably, because the spatial sampling of SRμCT is different from μMRI, the transformed position of each voxel may not coincide with the regular grid of the original image. Additionally, numerical truncation might force two or more voxels from the original volume to be transformed into the same voxel, thus producing empty voxels in the transformed volume. To avoid empty voxels in the transformed image, which alter the NMI, we implemented a reverse mapping procedure and trilinear interpolation (Sinibaldi et al., 2013).

Notably, we applied a specific downsampling/grouping strategy when estimating *NMI*, because the transformed and the target image must be sampled with the same spatial resolution. Each voxel in the down sampled SRμCT images has a value obtained as the average of a number of voxels equal to the ratio between the μMRI and the SRμCT 3D resolutions. Thus, the total number of voxels averaged in the 3D grouping window N_{3D}^{av} is

$$N_{3D}^{av} = \mathrm{int}\left(\prod_{i=1,3} \frac{\mathrm{lowRes}_i}{\mathrm{high\,Res}_i}\right),$$

where *i* denotes each of the three directions in the grid. In our case, N_{3D}^{av} was 88. Notably, because the sample and background volumes scanned by the two methods could not be exactly the same, the position of the 3D window on the SRµCT grid will determine the registration accuracy. Thus, during each minimization iteration, the 3D window can be translated on the high-resolution image to select the position of the downsampled grid centre providing the best registration accuracy. Thus, three additional subvoxel translation parameters were considered, and the number of trials for individuating the best tessellation was N_{3D}^{av}.

Eventually, a minimization run is performed for the different tessellations looking for the best set of parameters to maximize the NMI. During this optimization step, only three translational parameters are involved, hence downhill simplex method in multidimensions (Press et al., 1991) was employed instead of ASA. The output of the software was the stack of transformed high-resolution images coinciding with the low-resolution one. See Supporting Information for further details on the coregistration procedure.

2.7 | Multivariate 3D clustering

A multivariate clustering procedure (Chen, Luo, & Parker, 1998) was used to determine whether the different phases of bone structure and the different biological tissues could be automatically distinguished one from the other. This analysis was conducted on the registered SRµCT–µMRI stacks. A matrix comprising the grey values of all the voxels was created, and data were clustered through a modified version of the standard K-means procedure, developed for analyzing magneto-encephalographic data (Spadone, De Pasquale, Mantini, & Della Penna, 2012) and adapted for functional MRI data (Sestieri, Corbetta, Spadone, Romani, & Shulman, 2014). To avoid possible biases, the algorithm was modified to automatically estimate the cluster number through maximization of cluster size and based on measures of cluster validity (silhouette, Dunn Index and Davies-Bouldin Index as in Spadone et al., 2012).

Cluster analysis was first performed on the single reference slices corresponding to the microscopy images, to assign a label to each cluster through visual matching with the histological images. Then, cluster analysis was run on the whole 3D coregistered volumes (slice thickness of 200 µm), and cluster results on the reference slices were again compared with labelled ROIs in the histological image to allow voxel labelling throughout the sample volume. This procedure was repeated for the three samples.

3 | RESULTS

3.1 | SRµCT and µMR images

Sample axial slices acquired with both SRµCT and µMRI on the same cylindrical jawbone core are shown in Figure 1 for sample C-1. The SRµCT images were obtained with PR BPI (see in Figure S1 the same slices reconstructed through BPI without PR) and were endowed with high contrast between calcified tissues and marrow space. Additionally, a third phase representing tissues softer than calcified tissues

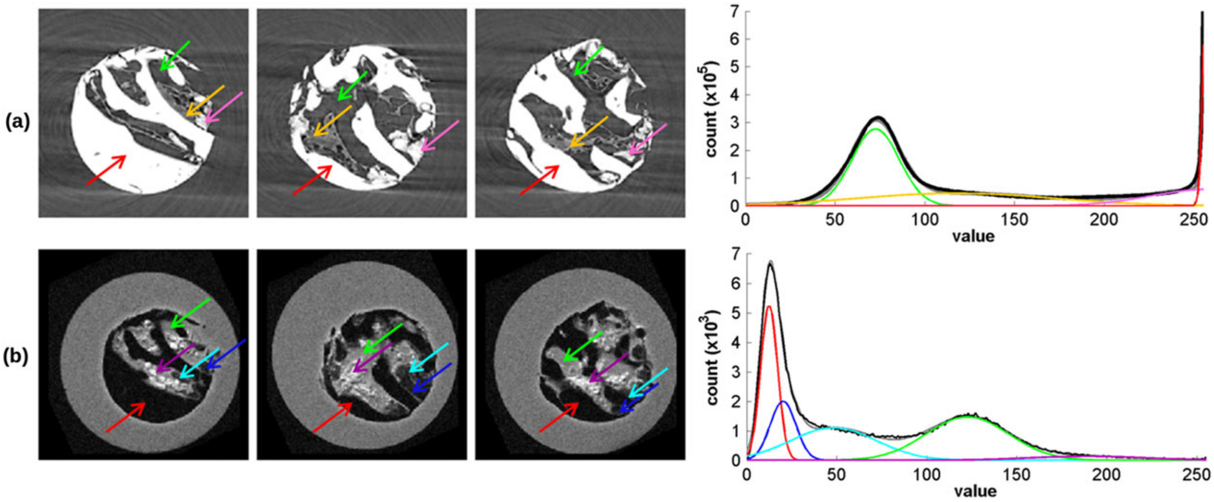

FIGURE 1 Left: Sample C-1, slices obtained by (a) PR BPI SRµCT and (b) µMRI. The spatial resolutions are 9 × 9 × 9 μm^3 for SRµCT and 18 × 18 × 200 μm^3 for µMRI. In the SRµCT images, a phase corresponding to calcified bone (red arrow), one to marrow space (green arrow) and two additional phases, possibly corresponding to soft biological tissue (orange arrow) and less calcified bone (pink arrow) can be visually detected. µMRI images show a good contrast between mature bone (red arrow) and marrow spaces (green arrow). Additionally, three phases, possibly corresponding to newly formed bone (blue and cyan arrows) and fat in the marrow space (violet arrow), can be visually disentangled. Right: (a) SRµCT and (b) µMRI histograms showing the grey scale distribution calculated on the whole 3D sample volumes. In (a), the experimental data (black line) are fitted (grey line) by the convolution of four distributions. However, although calcified bone (red line) and marrow space (green line) could be disentangled based on their distribution, it was not possible to separate the other two tissue types (orange and pink lines—see Table S1 for statistical comparisons). In (b), the experimental data (black line) are fitted (grey line) by the convolution of five distributions. However, only calcified bone is well separated from the marrow space and the bright areas

appears in the images together with a fourth phase, possibly related to less dense calcified bone. The distribution of the image grey values is shown in the related histogram (Figure 1a, right—thick black line), which was calculated over the whole sample volume and was deconvolved into four Gaussian populations (the theoretical estimate is in light grey). A statistical test versus the null hypothesis stating that pairs of Gaussian distribution were overlapped (p < .05), assessed whether the distance between the mean of a reference distribution and all the others, normalized to the standard deviation of the reference distribution, was >2.5. The test results are reported in Table S1. In summary, although four Gaussian distributions were needed to obtain a satisfying fit, the distribution of calcified tissue overlapped with the fourth phase, but they both differed from background and from the third phase, which overlapped with each other.

Figure 1b shows μMRI slices possibly matching with the SRμCT ones, obtained from the sample immersed in water and T_E = 4.8 ms, which produced the best contrast between different types of bone (in Figure S2, see the left slice in Figure 1b at different T_E). Despite the lower spatial resolution, μMRI disclosed a rich biological environment possibly composed by five different tissues. The grey tone reflects the dependence of T_2^{APP} on IMFG generated by the different bone mineral densities and on the restricted dynamics associated to water protons constricted in bone pores (De Santis et al., 2010; Rebuzzi et al., 2013). Thus, we expect signal from water in the trabecular space to produce brighter voxels, whereas water molecules fast decaying inside submicrometer pores embedded into bone matrix produce darker voxels. Highly porous phases corresponding to either newly formed bone or soft tissue (dark grey voxels) should appear at a grey tone lighter than calcified bone (black voxels). Finally, very bright areas overlapped on the light grey regions can be spotted on the MR image, whereas their counterparts were missing from the SRμCT images. We suppose that these bright signals were due to the partial overlap of signals produced by water and soft tissue rich in fatty molecules, adipocyte, or multinucleate cells (called fat in the following; Hardy, Henkelman, Bishop, Poon, & Plewes, 1992), brightening these voxels more than bulk water due to the different chemical shifts of water and fat (Hood, Ho, Smirniotopoulos, & Szumowski, 1999). Therefore, these bright areas cannot be exclusively linked to either fat or to water. The histogram obtained from the whole sample volume is displayed in Figure 1b, together with the deconvolution into five Gaussian populations. A statistical test similar to SRμCT (see Table S2 for results) stated that the distributions of more and less calcified bone tissues were partly overlapping. The water in the marrow space and the bright areas partly overlapped, but could be distinguished (p < .05) from the bone types.

3D morphometric parameters were estimated on both images and are described in Supporting Information.

Finally, in the two stacks of images no residues of the anorganic bovine biomaterial implanted in the patient jaw were clearly detectable.

In summary, Figure 1 suggests that SRμCT and μMRI alone only partially described the sample content although in a complementary way, suggesting the fusion of the two imaging methods to discriminate between different bone phases. This indication was supported by inspection of the coregistered images. The SRμCT stack was resampled at the slice thickness (each resampled slice was the average of 22 original slices) and resolution of μMRI before coregistration. Two sample slices of the coregistered SRμCT stack are shown in Figure 2a, b for sample C-1 (left μMRI, middle SRμCT) and in Figure S3 for samples C-2 and C-3. The overlap/nonoverlap between μMRI and the resampled and coregistered SRμCT images are reported in Figure 2 right, where the SRμCT images and the negative version of μMRI were

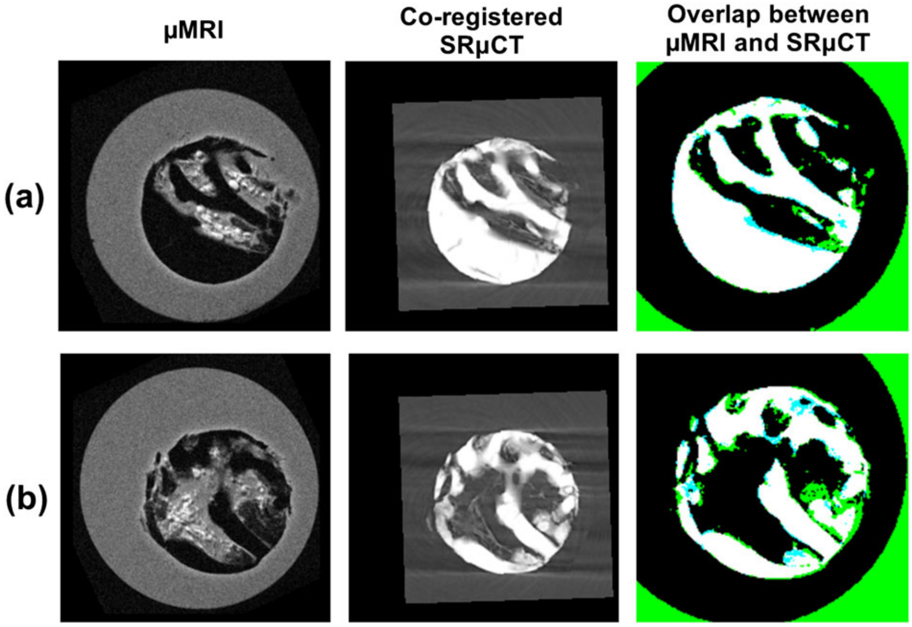

FIGURE 2 Sample C-1, two slices of the jawbone core are shown in (a) and (b): The μMR images (on the left) are compared to the corresponding coregistered SRμCT slices (in the centre), after their binarization. On the right the results of these comparisons: White and black indicate voxels where both the techniques reveal bone and background/marrow space, respectively. Green areas represent voxels which were detected as bone in μMRI and as background/marrow space in SRμCT, whereas cyan indicates the opposite case

binarized by applying a threshold at 195, and then overlapped. In the resulting image, white and black indicate overlap of bone tissue and marrow spaces/voids, respectively, detected by both techniques, although detailed structures within bone (new and calcified bone) and marrow spaces (soft tissue including fat) differ. Light green indicates voxels where only µMRI detects bone, whereas cyan voxels indicate the opposite case. The resulting image suggests that although a large number of voxels are ascribed to similar tissues by both methods, the overlay of the results of the two techniques evidences some differences among the structures. These results emphasize that merging the two techniques should improve the ability to detect bone micromorphology and composition in the jawbone.

3.2 | Histological evaluation

In order to compare the outcome of the multimodal 3D imaging with histology, two reference sections were taken from the bone core by cutting them at positions as close as possible to two corresponding slices imaged by µMRI (as this was the method with the worse axial resolution). The two images in Figure 3a are the histological references (thickness ~ 35 µm) for sample C-1 and roughly correspond to the left and middle slices shown in Figure 1 and to the upper and lower coregistered slices in Figure 2 (histological sections for sample C-2 and C-3 are shown in Figure S4).

According to criteria reported in Hayat, 1993, in Figure 3a, we can appreciate differential maturation within the bone tissue, comprising a mature trabecular structure, stained with dark blue and azure (labelled with B) and some areas of newly formed bone, stained with lighter blue and azure (labelled with NB). These areas are stained by different light blue tones and when observed at higher magnification (Figure 3—insert) reveal different types of tissue/structure. Presumably, they are covered by different osteoid seam thicknesses that is newly formed organic matrices less mineralized (Premkumar, 2011), thus suggesting the coexistence of two types of new bone with different amount of minerals and pores. In marrow spaces, we can spot dehydrated soft tissues picking a tiny amount of colour (DT) and small areas with debris (BD). The DT staining is irregular possibly due to an artefact determined by the dehydration shrinkage of the soft tissue. The BD can be individuated due to its morphology, consisting of tiny tissue pieces with irregular borders, separated from the other tissues, due to disaggregation of the bone matrix induced by the drilling process. No residual particles of anorganic bovine bone could be detected.

To allow labelling of different tissue regions on the coregistered stack (see next section), SRµCT was coregistered to each of the two stained histological sections independently (see Figure 3b). Before the SRµCT and histology coregistration, the optical microscopy images were downsampled to the in-plane resolution of SRµCT. During the coregistration procedure, the SRµCT image stack was resampled to a slice thickness of 36 µm by using the histological sample′s thickness as first guess. Thus, a voxel in the coregistered SRµCT–µMRI stack could be labelled through the application of two transformations: (a) an inverse transformation from the SRµCT stack coregistered with histology slice and (b) a transformation from the original SRµCT stack to the coregistered SRµCT-µMRI stack.

Notably, the SRµCT slices registered to the corresponding histological sections and the corresponding SRµCT slices registered to the µMRI stack (Figure 2, middle) do not overlap.

3.3 | SRµCT–µMRI image fusion

Following coregistration, a clustering algorithm was applied to the SRµCT–µMRI stack to group homologous voxels. Eventually, the resulting clusters were labelled according to the coregistered 2D optical microscopy. First, a 2D version of the multivariate clustering algorithm was run separately on the single slices roughly corresponding to the ones analysed by histological evaluation (Figure 3).

The algorithm output consisted of six clusters, and is shown in Figure 4a. These clusters, through comparison with the corresponding histological sections, suggested that merging µMRI and SRµCT images was able to disclose the following tissues: calcified bone, newly formed bone type I, newly formed bone type II, dehydrated soft tissue, fat, and marrow space/background. Qualitatively, these tissue types seem to be similar to the one shown by the histological images. Notably, the multivariate clustering on the coregistered images allowed to disentangle voxels comprising two phases of newly formed bone, which were detected by histological evaluation but were not revealed by µMRI and SRµCT when used separately.

Eventually, the multivariate grouping algorithm was applied to the sample volume (e.g., between the two reference slices of Figure 2 for sample C-1) and the 3D metastructure discloses high similarity to the 2D one obtained on the single slices. Figure 4b shows the clusters we obtained over the sample volume. In the 3D rendering, for sake of clarity, only the voxels representing the two types of newly formed bone are represented inside the sample volume, whereas detailed clustering results are displayed for three representative slices. Figure 4c contains the results of the cluster analysis for sample C-2, which can be compared with the related histological section in Figure S4a. For sample C-3, two slices of the 3D metastructure are shown in Figure 4d,e, because part of the histological section obtained from this sample (Figure S4b and S4c) corresponds to the slice in Figure 4d and the other part corresponds to Figure 4e. Notably, the clustering analysis for sample C-2 and C-3, supported by histological evaluation to label clusters, allowed identifying volumes of two types of new bone tissue as in sample C-1. In C-2, no fat tissue was clustered, as this tissue was not detected by µMRI, whereas in sample C-3, the dehydrated tissue was not detected.

We evaluated the precision of clustering over two groups of ROIs manually selected on the histological images downsampled at the resolution of µCT, one group clearly representing homogeneous bone tissues (10 ROIs) and the other clearly representing new bone tissues (10 ROIs). The selected ROIs are shown in Figure S5. Using the procedure described in Section 3.2, the ROIs highlighted in Figure S5 were transformed to the corresponding slice in the 3D metastructures. We then counted the fraction of voxels in the ROI included in each cluster. We averaged these values across ROI groups to evaluate the clustering precision. The overall clustering precision is 99.7% ± 0.7% for bone and 95% ± 5% for new bone. The larger standard deviation associated with the new bone tissue could also be driven by inhomogeneities in this type of tissue already detectable from histology. Using the same

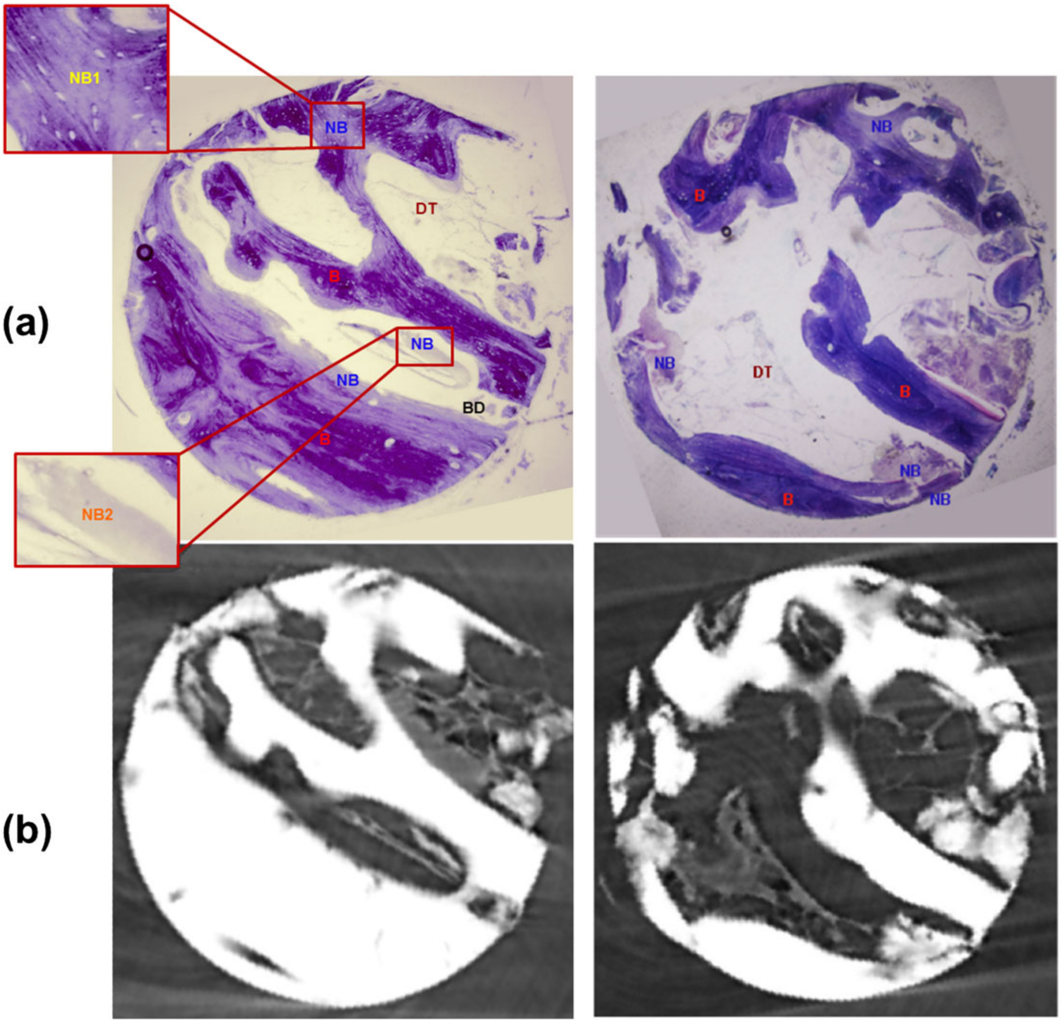

FIGURE 3 Sample C-1: (a) histological references with in plane resolution of 1.6 μm labelling calcified bone (B), newly formed bone (NB), dehydrated bone marrow (DT), and bone debris (BD) within the coregistered SRμCT slices. In the zoomed insets the presence of different types of newly formed bone, that is, more (NB1) and less mineralized (NB2) can be appreciated. (b) Co-registered images obtained by in-plane downsampling the optical microscopy photographs at the SRμCT resolution (9 μm) and by reducing the out-of-plane SRμCT resolution to the histological slice thickness (35 μm). The SRμCT images coregistered to these two histological sections are slightly different from the ones registered to the μMRI (see Figure 2)

procedure as describe above, we evaluated how the edge voxels were grouped by the clustering. We selected 10 ROIs representing bone edges and 10 ROIs representing new bone edges as revealed by the different colour tones in the histological images. We obtained the percentage of voxels grouped in accordance with the histological image is 91% ± 9% for bone edge and 90% ± 5% for new bone edge. These values are suggesting that possible biases of partial volumes are lower than 10% over the sample edge volumes.

We estimated the degree of mineralization for calcified bone and newly formed bone from the SRμCT images obtained by BPI reconstruction shown in Figure S1, where grey values correspond to HU. In the PR BPI images, the intensity values are no longer referred to HU. For each sample, we projected on the BPI images the voxels corresponding to the three types of bone. The mean grey values across volumes included in the same cluster were used to calculate the mineralization degree of the different bone types in the three samples. Mineralization of calcified bone was different across samples, with values 990 ± 320 mg/cm^3 for C-1, 770 ± 225 mg/cm^3 for C-2 and 915 ± 340 mg/cm^3 for C-3. The two newly formed bone types I and II assume very similar grey values on the BPI images. The mean degree of mineralization across all the new bone volumes in the three samples was 515 ± 270 mg/cm^3. Thus, the differentiation between the two types of new bone detected by the clustering is not driven by the mineralization degree alone and should be ascribed to the fusion of SRμCT and μMRI.

3.4 | 3D histomorphometry

As an example of a quantitative analysis of the 3D multivariate clustering output, we computed the tissue percentages for the three investigated samples, obtained from tissue volumes reported in Table S3. For each slice and each sample, we computed the volume fraction of the three mineralized tissues as the ratio between each mineralized phase and the total tissue volume (Komlev et al., 2010). This normalization

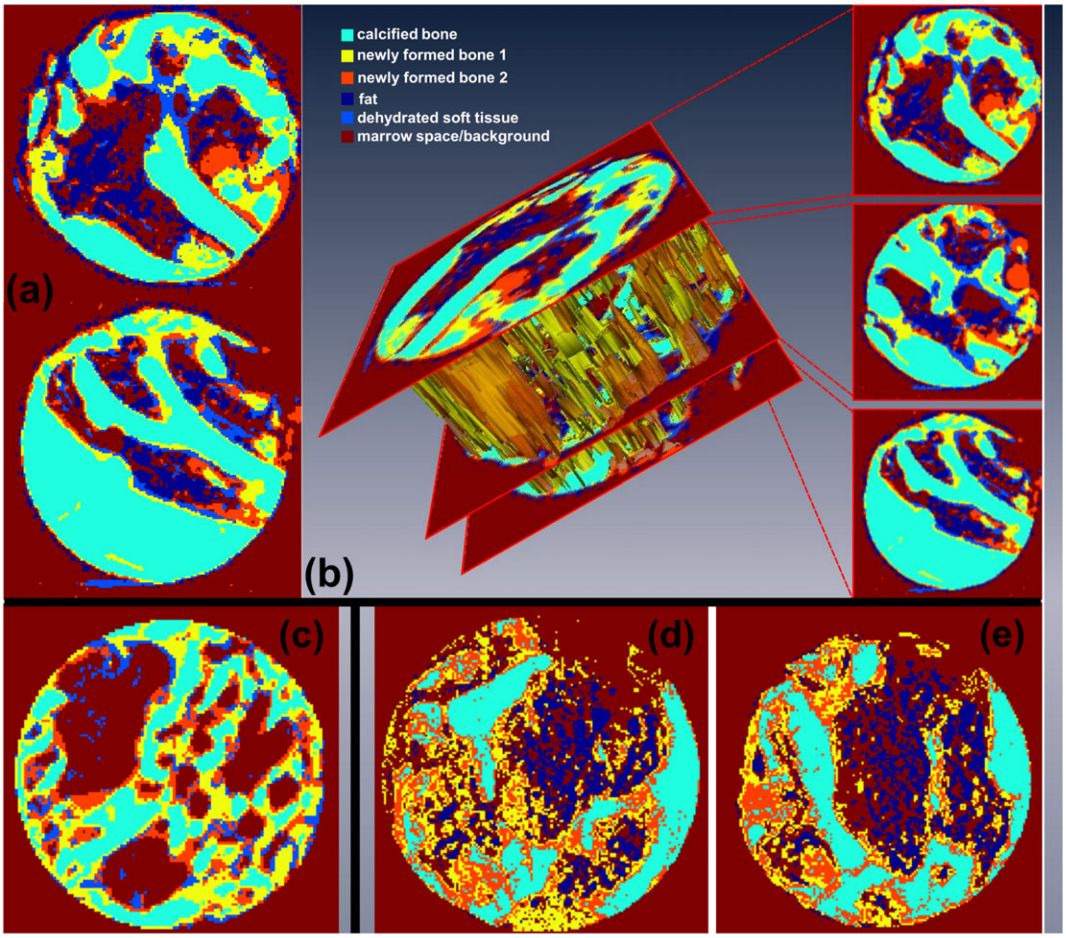

FIGURE 4 2D and 3D metastructures produced by the multivariate clustering of the coregistered µMRI-SRµCT images for the three samples. (a) Sample C-1, 2D metastructure for the slices corresponding to histological images. (b) 3D metastructure for the whole volume between the two slices of Figure 3. Both groupings disclose the same six clusters with the same distribution within the slices: calcified bone (cyan cluster), newly formed bone type I (yellow cluster), newly formed bone type II (orange cluster), dehydrated soft tissue (i.e., bone marrow; blue cluster), fat (dark blue cluster), and marrow space/background (brown cluster). For the sake of clarity, the 3D rendering in (b) shows only the semitransparent spatial distribution of the two newly formed bone clusters. The 3D image was obtained with Amira v. 4.1 (Mercury Computer System). On the right, the six clusters are displayed on the two reference slices corresponding to the histology sections and on a third slice within the sample volume.
(c) Representative slice from the 3D metastructure of sample C-2, corresponding to Figure S4a. (d) and (e) Representative slices from the 3D metastructure of sample C-3. Part of the histological section obtained from this sample (Figure S4b and S4c) corresponds to the slice in Figure 4d and the other part corresponds to Figure 4e

strategy allowed us to collapse the data from the three samples. In Figure 5, the volume fraction of NB1 and NB2, calculated for each slice of the 3D metastructures, are reported as a function of the volume fraction of the calcified bone. Specifically, a larger percentage of calcified bone corresponded to a smaller percentage of newly formed bone. Hence, these volume fractions of newly formed bone type I or II were fitted with a power law function. For the experimental data corresponding to the newly formed bone type I, the fitted equation was $y = 0.072x^{-1.2}$ ($R^2 = 0.56$), and for the newly formed bone type II, the equation was $y = 0.0195x^{-2.0}$ ($R^2 = 0.84$). Albeit these fits were run on a number of points probably too small to draw precise conclusion about the physiology of newly formed bone, they clearly show that quantification of relative new bone growth was possible over the whole volume without destroying the sample. Finally, a two-tail paired *t* test between the two fractions of the two types of new bone tissues suggested that the ratio for type I was always larger than type II ($p < 7*10^{-5}$).

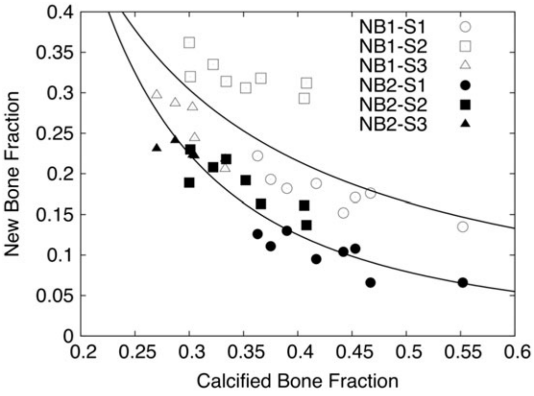

FIGURE 5 Volume fractions of newly formed bone type I (empty symbols) or II (filled symbols) as a function of calcified bone fraction. Data from the three samples are merged and shown with different symbol shapes. The continuous lines represent the power trends $y = 0.072x^{-1.2}$ ($R^2 = 0.56$) for NB1 and $y = 0.195x^{-2.0}$ ($R^2 = 0.84$), for NB2, respectively

4 | DISCUSSION

4.1 | Multimodal imaging for monitoring tissue regeneration

Cone beam X-ray computed tomography is the X-ray imaging gold standard in clinical practice (Dawood, Patel, & Brown, 2009) and is used in clinical trials to evaluate bone regeneration and to plan the surgery intervention. However, SRμCT and cone beam micro/nano X-ray tomography are actually the most powerful techniques to characterize the 3D structure of bone. With respect to cone beam, SRμCT can record subtle changes in attenuation across a wide range of tissue radiodensities, with a higher contrast thanks to the better uniformity of the incident X-ray beam over the area detector. These two powerful techniques can be employed on ex vivo bone cores, which can be retrieved during the implant bed preparation without any inconvinience to the patient and stored for further characterization. SRμCT alone is not able to provide a complete picture of bone tissue heterogeneity (Torrente et al., 2006), pushing towards support of SRμCT imaging through complementary techniques. Phase contrast tomography and X-ray microdiffraction were combined to investigate the crystalline phase associated to the newly formed bone, but required sectioning of the sample as well as histomorphometry (Cedola et al., 2014). Trabecular bone samples were analysed through correlation between MR T_2^* 3D relaxation maps and trabecular parameters separately estimated from μCT micromorphology (Wurnig et al., 2014).

In our approach, the detailed information on bone calcification using SRμCT and the information on bone chemical composition and matter physical state obtained by μMRI are integrated through multivariate clustering on coregistered images. The multimodal integration allowed to cluster two types of new bone tissue and disentangle them from calcified bone. This distinction was not possible on the images obtained by a single modality. Future implementation of the multimodal approach could include images from other independent technique, for example, small angle X-ray scattering tomography (Liebi et al., 2015), to reveal collagen volume fraction, fibre length and orientation (Buehler, 2006) or neutron scattering to improve the characterization of interfaces and submicrometre pores (Pozdnyakova et al., 2010).

4.2 | Quantitative assessment of regenerated tissue

When BSBs are implanted into a bone defect site, continuous tissue remodelling occurs, to achieve high vascularization degree, stable physiological conditions, optimal stiffness, and geometrical shapes (Rezwan, Chen, Blaker, & Boccaccini, 2006; Woodruff et al., 2012). Recently, different dynamics of tissue growth/maturation/remodelling were reported, suggesting that defects filled with immature tissue should not be considered regenerated although BSB was resorbed and an accurate differentiation among bone tissues would be fundamental to prevent implant failures (Traini et al., 2015; Woodruff et al., 2012).

In this study, we were able to disentangle mature from two types of new bone tissues. As the multivariate clustering allowed assigning every voxel of the coregistered image to a cluster, the 3D amount of the different bone tissue types could be quantitatively analysed. As an example, we found a power law between the volume fraction of new bone tissue types I and II versus the fraction of mature bone (Figure 5). Notably, fractions of fat and dehydrated tissue were approximately constant over the considered slices. Despite acknowledging that the exact relationship between the different bone fractions deserves further investigation due to the small data size, a decreasing trend between the new and calcified bone fractions is clearly shown in Figure 5. This trend could be compatible with bone regeneration processes, related to the local density of osteoclasts/osteoblasts. Specifically, during bone growth, osteoblasts are differentiated in osteocytes and embedded within the bone. This process implies a decrease of the osteoblasts number and a slowdown of the bone formation process, as the calcified bone matrix increases (Kini & Nandeesh, 2012). Similarly, when the osteoclast number decreases, new bone formation is reduced (Karsdal et al., 2007; Trubiani et al., 2010). The investigation of a larger number of samples would allow to analyse these power coefficients as a function of time and in different clinical protocols and to understand whether their values could be used as a marker of the regeneration process.

The multimodal tomographic approach proposed in this work discloses the possibility to detail and visualize 3D morphological structures embedded in bone samples and to differentiate tissue types that are detected as the same with one imaging technique alone. The possibility to reconstruct the sample in silicon with realistic 3D morphology is essential when running possible materials simulations resembling the real behaviour of the investigated bone structure (De Santis et al., 2010; Dejaco, Komlev, Jaroszewicz, Swieszkowski, & Hellmich, 2012).

Despite the higher spatial resolution of microscopy, histological sectioning cannot be used as input in numerical simulation to estimate biomechanical parameters such as bone strength or fracture toughness, as the input of these software tools should be a 3D volume with voxelwise labelling. The non-destructive character of the proposed investigation allows further spectroscopic and mechanical test following SRμCT and μMRI recordings. Notably, the use of different dyes allows to enhance the presence of different tissues, which could be contained or absent from the samples, but one selected dye does not allow to detect the whole tissue heterogeneity over the sample, neither it is possible to apply different dyes in sequence to detect features that are not disclosed by the first dye treatment.

4.3 | Methodological considerations

Our approach, based on the coregistration of images with different properties supported by multivariate clustering, could disentangle the newly formed from calcified bone. To assess how reliable are our results, we first evaluated the clustering precision. Despite the reduced image resolution of the 3D metastructure with respect to SRμCT and histology, the clustering precision was at least 95% when evaluated on homogeneous regions selected on histological images of the three samples. This value is fairly satisfying, although a voxelwise evaluation was not possible as a voxelwise labelling of histology in the field of bone tissue engineering is still a work in progress and could also produce biased results (Janssens et al., 2014). In addition, the stain we used is not able to detect all the tissue types obtained by cluster analysis of the coregistered images. Specific attention should be devoted to the partial volume effect on the 3D metastructure, partly due to the clustering precision and partly due to the handling of images with different resolution. Clustering precision evaluated on edge ROIs was >90%, with a standard deviation larger than homogeneous ROIs. In part, this precision, which was however large, was possibly affected by the difficulty, which sometimes affect the marking of a clear-cut edge between B and NB and between NB and DT on histology. In other part, it was also affected by the procedure used to evaluate the precision itself, which is influenced by the different resolution between histology and the fused images. In this perspective, as a contribution to the partial volume effects, it is important to discuss how the different properties of the two imaging methods might affect our results. The first issue is whether the considerably different resolution is efficaciously handled during the coregistration, because the large voxel size of μMRI requires that 22 SRμCT slices are averaged to obtain the same axial step of the μMRI grid. This procedure applied a spatial low pass filter to the SRμCT slices, smoothing trabeculae, and pores edges. What is the effect of the partial volumes on the "newly formed bone"? Despite acknowledging that part of the voxels comprised in the newly formed bone type I surround the calcified bone in Figure 4, and might be due to the partial volume effect, this part represents only a small subset of the voxels included in this cluster. Thus, its contribution to the morphometric parameters is negligible, as supported by the following considerations: (a) a large part of the voxels in the yellow cluster are placed far from the edge of the calcified bone and corresponded to new bone in the histological evaluation; if these voxels were clustered with the edge ones, then their tissue types should be robustly similar and could represent new bone tissue; (b) a large part of the voxels in the yellow cluster surrounding the cyan one correspond to the light green voxels in Figure 2, which are the voxels assumed as bone in μMRI only and thus do not correspond to the smoothed ones in SRμCT; (c) the negative power law between the newly formed bone type I and the calcified bone fractions suggests that most of voxels in the yellow cluster are not edge voxels, as the number of edge voxels would increase with the calcified bone fraction; (d) because also the newly formed bone type II, comprising voxels far from the mature bone edge, changes as a negative power law with the calcified bone fraction, the newly formed bone type I should not be driven by edge-smoothing effects. Similar arguments could also be applied against possible distortion effects introduced by μMRI (Duchin, Abosch, Yacoub, Sapiro, & Harel, 2012). In our case, the Field of View of the current system was small enough to ensure high homogeneity of the main and gradient fields. Finally, we do not expect that any distortion would produce a negative power law between the new bone tissue and the calcified bone fractions, but a relationship with a positive slope/power (the longer are the edges, the larger is the number of voxels involved in the distortion). Thus, despite we cannot exclude that slight distortion effects might affect the MR images, we assume that their contribution was negligible and could not generate the two new bone clusters.

The last methodological consideration discusses whether the specific clustering algorithm we here applied might produce the two new bone clusters, which do not correspond to real tissue differences. We applied a modified version of k-means (Spadone et al., 2012) suitable to cluster multivariate data. A limit of the standard k-means clustering is that the number of clusters should be user-selected, but in the actual version, the number of clusters is automatically selected using quantitative validity indices (Spadone et al., 2012). Thus, according to our algorithm, the partition of the new bone tissues into two clusters produces the best grouping and reducing the cluster number spoils the clustering performances. Then, the different exponents in the power law for the two new bone fractions suggest that the tissues are different, while we would expect the same power for the same type of tissue. We thus conclude that the two "new bone" clusters are reliable, as also confirmed by labelling through histology. Finally, in the actual implementation, we did not use classifiers, thus requiring histology of one slice for labelling the tissue types. In a future implementation of the whole pipeline, trained classifiers (e.g., self-organizing feature maps) using histological evaluation of a large number of samples as training data could be used to automatically recognize bone tissues at different mineralization degrees.

5 | CONCLUSIONS

In this paper, the data-driven analysis of specific 3D micromorphologies of different tissues composing an ex vivo human jawbone core was achieved applying multivariate clustering on the coregistered images obtained from two different non-destructive tomographic techniques, SRμCT and μMRI, and supported by 2D microscopy for tissue labelling.

By using the present, non-invasive approach, we were able to distinguish and to quantitatively analyse different types of newly formed bone from the calcified one, as confirmed by histological examinations. The technical aspects of the processing pipeline were accurately designed to provide a completely non-invasive and powerful tool for the coregistration and analysis of multimodal images. Specifically, the introduction of a 3D floating grouping window increased registration accuracy. The multivariate clustering algorithm with the automatic selection of the cluster number allowed the data-driven identification of different biological tissues, suggesting different types of new bone emerging during the bone maturation process. It is very important to evaluate the bone tissue heterogeneity and its distribution over the sample volume. This information allows to know how different tissues and mineral density are distributed inside the sample, which are needed to estimate the bone strength. This estimate is not possible from the measure of the average bone mineral density using only X-ray tomography, which does not exactly disentangle the two new bone tissues from soft tissue. On the other side, the estimation of failure risk would benefit from the 3D distribution of tissues obtained from the 3D metastructure.

ACKNOWLEDGEMENTS

This work was partially supported by the Special Multiaxis Project "Networks for high education" P.O. F.S.E. Abruzzo 2007–2013.

CONFLICT OF INTEREST

There are no conflicts of interest, and there are no prepublished information or materials in this manuscript.

ORCID

R. Sinibaldi http://orcid.org/0000-0002-2137-2351

S. Della Penna http://orcid.org/0000-0001-5067-4327

REFERENCES

Buehler, M. J. (2006). Nature designs tough collagen: Explaining the nanostructure of collagen fibrils. *PNAS*, *103*, 12285–12290.

Cedola, A., Campi, G., Pelliccia, D., Bukreeva, I., Fratini, M., Burghammer, M., … Mastrogiacomo, M. (2014). Three dimensional visualization of engineered bone and soft tissue by combined x-ray micro-diffraction and phase contrast tomography. *Physics in Medicine and Biology*, *59*, 189–201.

Chee, W., & Jivraj, S. (2007). Failures in implant dentistry. *British Dental Journal*, *202*, 123–129.

Chen, C. W., Luo, J., & Parker, K. J. (1998). Image segmentation via adaptive-mean clustering and knowledge-based morphological operations with biomedical applications. *IEEE Transactions on Image Processing*, *7*, 1673–1683.

Dawood, A., Patel, S., & Brown, J. (2009). Cone beam CT in dental practice. *British Dental Journal*, *207*, 23–28.

De Santis, S., Rebuzzi, M., Di Pietro, G., Maraviglia, B., & Capuani, S. (2010). In vitro and in vivo MR evaluation of internal gradient to assess trabecular bone density. *Physics in Medicine and Biology*, *55*, 5767–5785.

Dejaco, A., Komlev, V. S., Jaroszewicz, J., Swieszkowski, W., & Hellmich, C. (2012). Micro CT-based multiscale elasticity of double-porous (pre-cracked) hydroxyapatite granules for regenerative medicine. *Journal of Biomechanics*, *45*, 1068–1075.

Di Pietro, G., Palombo, M., & Capuani, S. (2014). Internal magnetic field gradients in heterogeneous porous systems: Comparison between Spin-Echo and Diffusion Decay Internal Field (DDIF) method. *Appl Magn Res*, *45*, 771–784.

Duchin, Y., Abosch, A., Yacoub, E., Sapiro, G., & Harel, N. (2012). Feasibility of using ultra-high field (7 T) MRI for clinical surgical targeting. *PloS One*, *7*, e37328.

Farr, J. N., Drake, M. T., Amin, S., Melton, L. J. 3rd, McCready, L. K., & Khosla, S. (2014). In vivo assessment of bone quality in postmenopausal women with type 2 diabetes. *Journal of Bone and Mineral Research*, *29*, 787–795.

Fritsch, H. (1989). Staining of different tissue in thick epoxy resin-impregnated sections of human fetuses. *Stain Technology*, *64*, 75–79.

Genant, H. K., Engelke, K., Fuerst, T., Glüer, C. C., Grampp, S., & Harris, S. T. (1996). Non invasive assessment of bone mineral and structure: State of the art. *Journal of Bone and Mineral Research*, *11*, 707–730.

Giannoni, P., Mastrogiacomo, M., Alini, M., Pearce, S. G., Corsi, A., Santolini, F., … Cancedda, R. (2008). Regeneration of large bone defects in sheep using bone marrow stromal cells. *Journal of Tissue Engineering and Regenerative Medicine*, *2*, 253–262.

Gureyev, T., Mohammadi, S., Nesterets, Y., Dullin, C., & Tromba, G. (2013). Accuracy and precision of reconstruction of complex refractive index in near-field single-distance propagation-based phase-contrast tomography. *Journal of Applied Physics*, *114*, 114906.

Hardy, P. A., Henkelman, R. M., Bishop, J. E., Poon, S. C., & Plewes, D. B. (1992). Why fat is bright in RARE and fast spin-echo imaging. *Journal of Magnetic Resonance Imaging*, *2*, 533–540.

Hayat, M. A. (1993). *Stain and cytochemical methods*. New York, NY, USA: Plenum Publishing Corp.

Hellmich, C., Kober, C., & Erdmann, B. (2008). Micromechanics-based conversion of CT data into anisotropic elasticity tensors, applied to FE simulations of a mandible. *Annals of Biomedical Engineering*, *36*, 108–122.

Hood, M. N., Ho, V. B., Smirniotopoulos, J. G., & Szumowski, J. (1999). Chemical shift: The artifact and clinical tool revisited. *Radiographics*, *19*, 357–371.

Janssens, T., Vanhees, I., Gunst, J., Owen, H., Van den Berghe, G., & Güiza, G. F. (2014). Automated histological quantification of trabecular bone tissue in critical illness. MIUA 229-234.

Karsdal, M. A., Martin, T. J., Bollerslev, J., Christiansen, C., & Henriksen, K. (2007). Are non resorbing osteoclasts sources of bone anabolic activity? *Journal of Bone and Mineral Research*, *22*, 487–494.

Khosla, S., Riggs, B. L., Atkinson, E. J., Oberg, A. L., McDaniel, L. J., Holets, M., … Melton, L. J. 3rd. (2006). Effects of sex and age on bone microstructure at the ultradistal radius: A population based non-invasive in vivo assessment. *Journal of Bone and Mineral Research*, *21*, 124–131.

Kierman, J. A. (2010). ‘General oversight stains for histology and histopathology’ in Special Stains and H & E, GL Kumar and JA Keirman eds, Dako North America, Carpinteria, CA, USA

Kini, U., & Nandeesh, B. N. (2012). *“Physiology of bone formation, remodeling, and metabolism” in radionuclide and hybrid bone imaging*. Berlin, Germany: Springer.

Komlev, V. S., Mastrogiacomo, M., Pereira, R. C., Peyrin, F., Rustichelli, F., & Cancedda, R. (2010). Biodegradation of porous calcium phosphate scaffolds in an ectopic bone formation model studied by X-ray computed micro-tomography. *European Cells and Materials*, *19*, 136–146.

Liebi, M., Georgiadis, M., Menzel, A., Schneider, P., Kohlbrecher, J., Bunk, O., & Guizar-Sicairos, M. (2015). Nanostructure surveys of macroscopic specimens by small-angle scattering tensor tomography. *Nature*, *527*, 349–352.

Miri, A. K., Muja, N., Kamranpour, N. O., Lepry, W. C., Boccaccini, A. R., Clarke, S. A., & Nazhat, S. N. (2016). Ectopic bone formation in rapidly fabricated acellular injectable dense collagen-Bioglass hybrid scaffolds via gel aspiration-ejection. *Biomaterials*, *85*, 128–141.

Pozdnyakova, A., Giuliani, A., Dutkiewiczz, J., Babutsky, A., Chyzhyk, A., Roether, J. A., … Ortore, M. G. (2010). Analysis of porosity in NiTi SMA's changed by secondary pulse electric current treatment by means of ultra small angle scattering and micro-computed tomography. *Intermetallics*, *18*, 907–912.

Premkumar, S. (2011). *Textbook of craniofacial growth*. New Delhi, India: Jaypee Publishers.

Press, W. H., Flannery, B. P., Teukolsky, S. A., & Vetterling, W. T. (1991). *Numerical recipes in C*. Cambridge, UK: Cambridge University Press.

Rebuzzi, R., Vinicola, V., Taggi, F., Sabatini, U., Wehrli, F. W., & Capuani, S. (2013). Potential diagnostic role of the MRI-derived internal magnetic field gradient in calcaneus cancellous bone for evaluating postmenopausal osteoporosis at 3 T. *Bone*, *57*, 155–163.

Rezwan, K., Chen, Q. Z., Blaker, J. J., & Boccaccini, A. R. (2006). Biodegradable and bioactive porous polymer/inorganic composite scaffolds for bone tissue engineering. *Biomaterials*, *27*, 3413–3431.

Sestieri, C., Corbetta, M., Spadone, S., Romani, G. L., & Shulman, G. L. (2014). Domain-general signals in the cingulo-opercular network for visuospatial attention and episodic memory. *Journal of Cognitive Neuroscience*, *26*, 551–568.

Sievanen, H., Kannus, P., & Jarvinen, T. L. N. (2007). Bone quality an empty term. *PLoS Medicine*, *4*, 407–410.

Sinibaldi, R., Conti, A., Pecci, R., Plotino, G., Guidotti, R., Grande, N. M., … Della Penna, S. (2013). Software tools for the quantitative evaluation of dental treatment effects from µCT scans. *Journal of Biomedical Graphics and Computing*, *3*, 85–100.

Spadone, S., De Pasquale, F., Mantini, D., & Della Penna, S. (2012). A K-means multivariate approach for clustering independent components from magnetoencephalographic data. *NeuroImage*, *62*, 1912–1923.

Studholme, C., Hill, D. L. G., & Hawkes, D. J. (1999). An overlap invariant entropy measure of 3D medical image alignment. *Pattern Recognition*, *32*, 71–86.

Torrente, Y., Gavina, M., Belicchi, M., Fiori, F., Komlev, V., Bresolin, N., & Rustichelli, F. (2006). High resolution X-ray microtomography for three-dimensional visualization of human stem cell muscle homing. *FEBS Letters*, *580*, 5759–5764.

Torres, F. G., Nazhat, S. N., Sheikh, S. H., Fadzullah, M., Maquet, V., & Boccaccini, A. R. (2007). Mechanical properties and bioactivity of porous PLGA/TiO2 nanoparticle-filled composites for tissue engineering scaffolds. *Composites Science and Technology*, *67*, 1139–1147.

Traini, T., Piattelli, A., Caputi, S., Degidi, M., Mangano, C., Scarano, A., … Iezzi, G. (2015). Regeneration of human bone using different bone substitute biomaterials. *Clinical Implant Dentistry and Related Research*, *17*, 150–162.

Tromba, G., Longo, R., Abrami, A., Arfelli, F., Astolfo, A., Bregant, P., … Castelli, E. (2010). The SYRMEP beamline of Elettra: Clinical mammography and biomedical applications. *AIP Conference Proceedings*, *1266*, 18–23.

Trubiani, O., Fulle, S., Traini, T., Paludi, M., La Rovere, R., Orciani, M., … Piattelli, A. (2010). Functional assay, expression of growth factors and proteins modulating bone-arrangement in human osteoblasts seeded on an anorganic bovine bone material. *European Cells and Materials*, *20*, 72–83.

Vandoorne, K., Magland, J., Plaks, V., Sharir, A., Zelzer, E., Wehrli, F., … Neeman, M. (2010). Bone vascularization and trabecular bone formation are mediated by PKB alpha/Akt1 in a gene-dosage-dependent manner: In vivo and ex vivo MRI. *Magnetic Resonance in Medicine*, *64*, 54–64.

Withers, P. J. (2007). X-ray nanotomography. *Materials Today*, *10*, 26–34.

Woodruff, M. A., Lange, C., Reichert, J., Berner, A., Chen, F., Fratzl, P., … Hutmacher, D. W. (2012). Bone tissue engineering from bench to bedside. *Materials Today*, *15*, 430–435.

Wurnig, M. C., Calcagni, M., Kenkel, D., Vich, M., Weiger, M., Andreisek, M., … Boss, A. (2014). Characterization of trabecular bone density with ultra-short echo-time MRI at 1.5, 3.0 and 7.0 T—Comparison with micro-computed tomography. *NMR in Biomedicine*, *27*, 1159–1166.

SUPPORTING INFORMATION

Additional Supporting Information may be found online in the supporting information tab for this article.

Figure S1 The SRμCT slices obtained by Back Projection Imaging (BPI) reconstruction without pre-processing were less detailed than the ones obtained by Phase Retrieval BPI reconstruction. These figures demonstrate that it is hard to disentangle low mineralized bone and soft tissues from bone trabeculae. As a matter of facts, the related histogram was fitted by 3 distributions (not shown) with just one common peak describing both tissues.

Figure S2 A sample slice displayed at different TE. At TE = 4.8 ms (which is the one used for further processing) the highest contrast between different tissues is obtained.

Table S1 Relative distance between distributions obtained from PR BPI SRμCT. The histogram on which the Gaussian populations were deconvolved was obtained over the sample volume only. The relative distance is expressed as the ratio between the absolute value of the distance of the two means and the standard deviation of the reference distribution (the first letter in each of the "Distribution" boxes). Coding: G = Green, O = Orange, P = Pink, R = Red. In bold we highlight the comparisons which were below statistical significance ($p < 0.05$). Distribution pairs were assumed as overlapping when the null hypothesis was verified in one of the two comparisons (a reference distribution vs the other and/or the other way round).

Table S2 Relative distance between distributions obtained from μMR images. The histogram on which Gaussian population s were deconvolved was obtained over the sample volume only. The relative distance is expressed as the ratio between the absolute value of the distance of the two means and the standard deviation of the reference distribution (the first letter in each of the "Distribution" boxes). Coding: G = Green, B = Blue, C = Cyan, R = Red, V = Violet. In bold we highlight the comparisons which were below statistical significance ($p < 0.05$). Distribution pairs were assumed as overlapping when the null hypothesis was verified in one of the two comparisons (a reference distribution vs the other and/or the other way round).

Table S3 Slice-specific volume number for each of the clusters detected by the 3D multivariate-grouping algorithm in the three samples.

Figure S3 μMRI (left side) and SRμCT (right side) images of samples C-2 (a) and C-3 (b, c). The gray values in the SRμCT image of sample C-2 are lower than the other samples, possibly due to a lower mineralization degree in the bone tissues.

Figure S4 Histological sections (left side) and clustering results (right side) for sample C-2 (a) and C-3 (b). The histological section of sample C-3 matches on two different slices of the 3D metastructure obtained through clustering.

Figure S5 Rois selected in the histology slice to evaluate precision of clustering. (a) and (b) sample C-1, (c) sample C-2, (d) sample C-3. The latter is divided in two parts because left and right side match on two different slices of the 3D metastructure**.**

How to cite this article: Sinibaldi R, Conti A, Sinjari B, et al. Multimodal-3D imaging based on μMRI and μCT techniques bridges the gap with histology in visualization of the bone regeneration process. *J Tissue Eng Regen Med*. 2018;12:750–761. https://doi.org/10.1002/term.2494